

Near-field antenna pattern measurement and holographic phase retrieval of a LiteBIRD high frequency telescope optical model

Emile Carinos^a, Hayato Takakura^b, Yutaro Sekimoto^b, Baptiste Mot^a, Ludovic Montier^a, Rion Takahashi^c, Hiroaki Imada^d for the *LiteBIRD* Collaboration

^aIRAP, Toulouse, France

^bJapan Aerospace Exploration Agency, Institute of Space and Astronautical Science, Sagamihara, Kanagawa, Japan

^cThe University of Tokyo, School of Science, Department of Astronomy, Bunkyo-ku, Tokyo, Japan

^dNational Astronomical Observatory of Japan, Mitaka, Tokyo, Japan

ABSTRACT

B-mode polarization detection in the Cosmic Microwave Background would provide crucial information on the inflationary universe. This is the main goal of the *LiteBIRD* JAXA-led space mission, to be launched by the beginning of the 2030s. To do so it is necessary to control instrumental systematics such as contamination from the far sidelobes of the telescopes. Following the studies that have been done for *LiteBIRD*'s Low Frequency Telescope (LFT), we measured near-field antenna patterns of a High Frequency Telescope (HFT) optical prototype to showcase the capabilities for the HFT of near-field antenna pattern measurement as well as holographic phase retrieval. We were able to characterize the far-field antenna pattern up to $\theta = 60^\circ$ with a dynamic range of -80 dB. The residuals were estimated to be at most 5 dB at the -80 dB detection level. We detected far sidelobes at $\theta \approx 30^\circ$ with a relative intensity of -50 dB, in line with previous simulations of the HFT. Holographic phase retrieval and other time-frequency analysis of the data show promising results for the characterization of the HFT.

Keywords: Cosmic Microwave Background, Near-Field Vector Measurements, Holographic Phase Retrieval, LiteBIRD, Time Frequency Analysis, Wavelets

Contents

1	Introduction	2
2	Methodology	2
2.1	Near-Field Vector Measurements	2
2.2	Holographic phase retrieval	3
2.3	Time Domain and Frequency-Time Analysis	4
3	Measurement setup	4
3.1	HFT Optical Prototype	4
3.2	Setup at ISAS	6
3.3	Data Reduction	7

Further author information: (Send correspondence to Emile Carinos)

Emile Carinos: E-mail: emile.carinos@irap.omp.eu

4	Results	7
4.1	Near-Field	7
4.2	Holographic	8
5	Discussion	11
5.1	Setup Reliability	11
5.1.1	Residuals	11
5.1.2	Side lobe patterns	12
5.1.3	Frequency-Time Analysis	13
5.2	Comparison with simulations	14
6	Conclusion	15

1. INTRODUCTION

A detection of B-mode polarization in the Cosmic Microwave Background (CMB) anisotropies could provide critical information on the early stages of the Universe, as predicted by inflation theory.^{1,2} The key metric for this detection is the tensor-to-scalar ratio r , parameterizing the relative importance of tensor modes over scalar modes. A number of CMB experiments are targeting the detection of such signals, with the current best upper limit being $r < 0.032$.³ In this context, the LiteBIRD mission^{4,5} is a JAXA-led Strategic Large-Class mission selected by ISAS/JAXA in 2019 to be launched by the beginning of the 2030s, and aimed at mapping the cosmic microwave background (CMB) polarized emission over the full sky at large angular scales. It consists in 15 broad bands distributed into three instruments (LFT, MFT and HFT) covering a large range of frequencies, from 37 to 448 GHz. This satellite mission proposes to achieve an unprecedented sensitivity on r , i.e. $\delta_r < 0.001$. The challenging scientific requirements of LiteBIRD imply stringent technical requirements to reach an unprecedented control of the instrumental systematic effects, especially since LiteBIRD mainly targets the largest scales over the sky (multipoles $2 < \ell < 200$). One of those instrumental systematic effects is the knowledge of the beam pattern, especially for the far side lobes, for which very stringent requirements have been settled, even more stringent in the highest frequency bands.⁶ A new technique has been demonstrated on the Low Frequency Telescope (LFT) to measure the far-side lobe features at warm temperature using near-field vector measurements^{7,8} and holographic phase-retrieval.⁹ This technique appears extremely promising, since it requires only a very compact facility and it could be applied to the characterisation of a whole focal plane populated with TES detectors, instead of using adhoc VNA setups at specific locations of the aperture. While the LFT optics follows a cross-dragone scheme, the mid- and high-frequency telescopes (MFT and HFT) have been designed as fully transmissive optics.¹⁰ We present in this paper the results of the first test campaign during which we performed similar near-field vector measurements and holographic phase-retrieval on a prototype of the HFT, using a very similar setup than the one used for the LFT. Some specific care has been given to the characterisation of the reliability and stability of the measurements setup as well as the development of specific analysis tools to dig into this frequency-time data flow.

2. METHODOLOGY

2.1 Near-Field Vector Measurements

In order to characterize the angular response of an antenna across wide ranges in the far-field regime, we can measure on a plane grid its amplitude and phase response in the near-field regime. This allows for simple and compact measurement setups to be developed. The principle of such a measurement relies on the Fourier transform (11, 12). As developed in Ref. 9, the antenna pattern $F(u, v, \omega)$ in planar spatial-frequency coordinates (u, v) is related to the near-field complex amplitude following :

$$F(u, v, \omega) \propto \iint E(x, y, \omega) e^{jk(ux+vy)} dx dy, \quad (1)$$

where $E = |E|e^{j\phi}$ is the near-field vector measured, x and y are the planar coordinates, $\omega = 2\pi f$ is the wave's angular frequency. The Fourier coordinates (u, v) are related to the spherical angular coordinates (θ, ϕ) , that are commonly used to describe a 3D antenna pattern, following these relations :

$$u = \sin \theta \sin \phi, v = \sin \theta \cos \phi \quad (2)$$

In order to plot F , we chose the polar spherical phi over theta positioning system, as described in Ref. 12.

2.2 Holographic phase retrieval

Both the amplitude and the phase information of the near-field signal are used to properly retrieve the far-field antenna pattern in the case of near-field vector measurements. Thus, this method relies on having a probe antenna that can measure both the phase and the amplitude of the signal. However, the Transition Edge Sensors that will be used as LiteBIRD's detectors¹³ are only sensitive to the intensity of the signal. In order to solve this problem, we can use interferometrical methods such as holographic phase reconstruction. This has already been used for a prototype of LiteBIRD's Low Frequency Telescope⁹ and the method we describe here is the same as the one used for these measurements. A reference signal E_{ref} , for which we know its intensity and phase, sent along with the signal coming from the aperture E_{sig} of the tested antenna will produce a measured intensity signal $H = |E_{sig} + E_{ref}|^2$ that we call the hologram. Such a setup is illustrated in figure 1.

From there we can develop H 's expression :

$$H(r, \omega) = |E_{sig} + E_{ref}|^2 = |E_{sig}|^2 + |E_{ref}|^2 + E_{sig}E_{ref}^* + E_{sig}^*E_{ref} \quad (3)$$

The two intensity terms can be obtained by performing additional near-field measurements with the reference or the probe turned off. We are left with two cross-correlation terms¹⁴ containing the information we are looking for : the complex amplitude of the signal E_{sig} . We can make use of the fact that we are measuring these holograms at different frequencies in order to separate these two terms. Indeed, by taking the inverse Fourier transform of $H' := H(r, \omega) - |E_{sig}(r, \omega)|^2 - |E_{ref}(r, \omega)|^2$ with respect to ω we get :

$$h'(r, t) = e_{sig}(r, t) * e_{ref}^*(r, t) + e_{sig}^*(r, t) * e_{ref}(r, t) \quad (4)$$

The two terms being complex conjugates of one another, we have $e_{sig} * e_{ref}^*(r, t) = e_{sig}^* * e_{ref}(r, -t)$. With the condition that the Fourier transform of the cross-correlation terms is simple enough we can thus define a window function $w(r, t)$ so that

$$h'_{filt} = h'(r, t) * w(r, t) \approx e_{sig}(r, t) * e_{ref}^*(r, t) \quad (5)$$

Then we can Fourier transform h'_{filt} into the frequency domain and define an estimation of E_{sig} as :

$$E_{sig}^{retrieved}(r, \omega) = \frac{H'_{filt}}{E_{ref}^*} \quad (6)$$

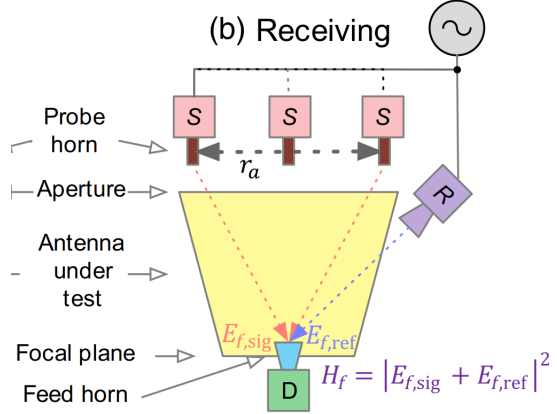


Figure 1. Setup for holographic measurements, adapted from 9. The antenna we are testing is the HFT optical prototype, it is set to be in receiving mode in our setup. The probe horn moves across the XY plane to scan the near-field pattern while the reference antenna R stays at the same position throughout the measurement.

2.3 Time Domain and Frequency-Time Analysis

The holographic phase-retrieval method relies on the fact that we have a multi-frequency observation at each point in the near-field plane to retrieve additional information about the signal using the Fourier transform to look at the data in the time-delay domain. This information has been used¹⁵ to characterize and filter out straylight components, or filter out the conjugate term in the holographic method. The ideal case of having $h'(r, t)$ being a simple time-delay spectrum containing only two well separated peaks is far from reality. Time delays can be different for each frequency of observation, and effects such as straylight, stationary waves or multiple reflections in the optical system can result in a more complex structure of the time-delay spectrum. Moreover, time-domain analysis of a multi-frequency observation using the Fourier transform has some limitations,¹⁶ especially when it comes to the *localization* of the time-domain features for each frequency. Non-stationary time delays will be detected but using only the Fourier transform we won't know at which frequencies they happen. Since we want to characterize each band of observation with the best precision, we need a better localization in the frequency domain. This can be provided by time-frequency analysis (or, in our case, frequency-time) methods such as the Continuous Wavelet Transform (CWT)¹⁷ or the Short-Time Fourier Transform (STFT). This kind of analysis has been extensively used in different domains of data analysis to better localize spectral information in both time and frequency domains,¹⁸ and in our case can provide an interesting diagnostic of the behaviour of the antenna and optical system for each frequency band.

3. MEASUREMENT SETUP

3.1 HFT Optical Prototype

The HFT Optical prototype, see figure 2, has been developed to replicate the optical properties of the HFT telescope, designed specifically for operation at ambient temperatures in contrast to the cryogenic environment of the HFT. Mainly composed of two lenses, optical and RF absorbers, and of a mechanical structure, this prototype replicates the HFT telescope's optical behavior.



Figure 2. The Optical and RF prototype of LiteBIRD MHFT.

Fabricated from High Density PolyPropylene, the two lenses are engineered to closely resemble the optical characteristics of the cryogenic lenses within the HFT telescope when operating under warmer conditions. This ensures that the prototype accurately mimics the characteristics of the telescope.

During the characterization campaign, two distinct types of absorbers were utilized to effectively manage the stray light. The first type employs CR110 tiles positioned around the mechanical tube, while the second type incorporates ecosorb AN-72 panels in place of the tiles, see figure 3.

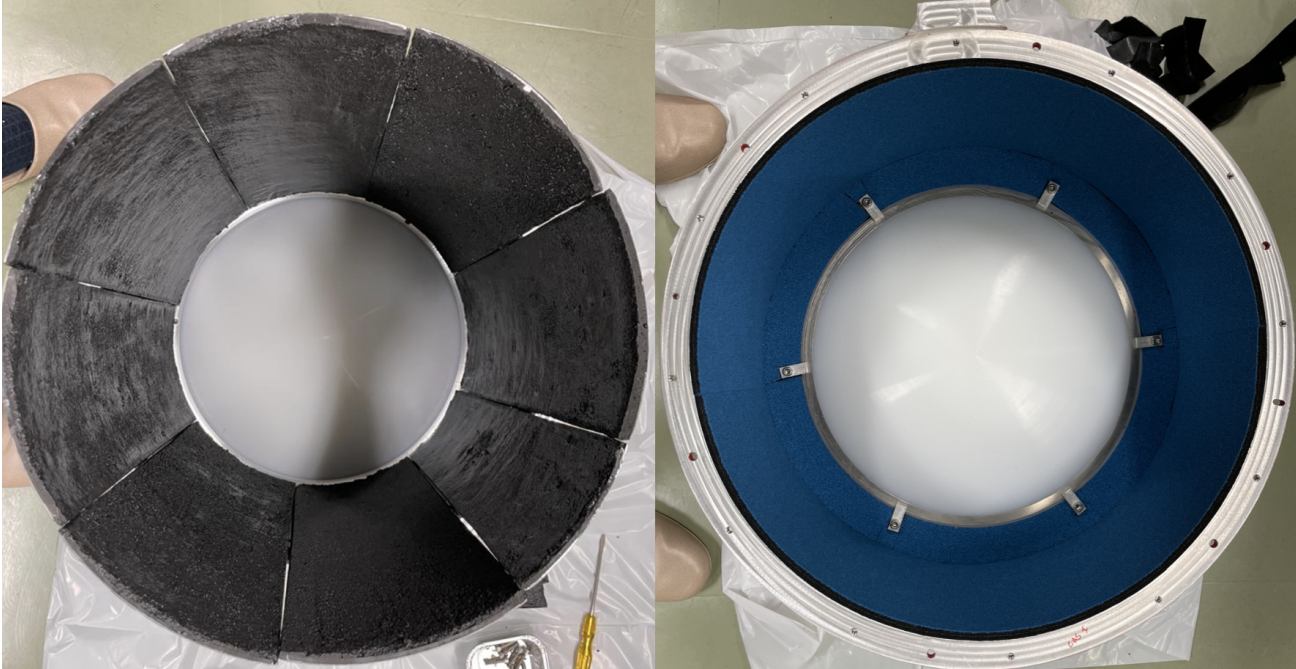


Figure 3. Absorbers used during the characterisations, Left CR110 tiles, Right AN-72 panels.

The mechanical structure, constructed from aluminum, serves as the framework for the prototype, providing essential support for the optical elements and absorbers. Additionally, this structure integrates several mechanical references, facilitating the optical alignments and ensuring the accurate positioning of the prototype with relation to the optical test bench.

3.2 Setup at ISAS

We measured the antenna patterns of the ORFPM using planar near-field measurement method (e.g., Ref. 12). To scan the aperture fields of the ORFPM, we used a vector network analyzer (VNA; Keysight N5222B) with frequency-extention modules (transmitter and receiver; Virginia Diodes WR5.1VNAX) and motorized stages. The near-field measurement setup is based on the one developed for measurements of the LFT prototypes.^{7,9,15} The ORFPM was measured as a receiving antenna. The measurements were performed at room temperature.

Figure 4 illustrates the measurement setup used in this experiment. The VNA transmitter with the probe horn is moved by the XY stages and scans the aperture of the ORFPM. The probe horn is an open-ended rectangular waveguide whose aperture size is 1.2954 mm × 0.6477 mm. To reduce the standing waves, absorber sheets (Eccosorb AN-72) are placed around the stages. In addition, an absorber tile (Thomas-Keating THz RAM) is attached at the aperture of the probe horn. The signal is detected at the VNA receiver with the feed horn (a corrugated conical horn) at the focal plane. The corrugated feed horn is designed such that its beam widths become similar to those planned for the sinuous-lenslet feeds for the LFT.⁸ The feed position can be adjusted by the XYZ stages. Between the feed horn and receiver, a polarization switch is inserted so that the feed polarization can be rotated.

For the holographic phase-retrieval measurements, we turn on the signal from the reference horn (a smoothed-wall conical horn with an aperture diameter of 8.33 mm and a length of 19 mm), which is phase-locked with the signal from the probe horn, so that these two signals generate interferometric fringes (holograms) at the focal plane.⁹ The optical axis of the reference horn is tilted from that of the ORFPM by 46.3°. Although the VNA measures both the intensity and phase of the detected signals, we only use the intensity information for the phase-retrieval computation.

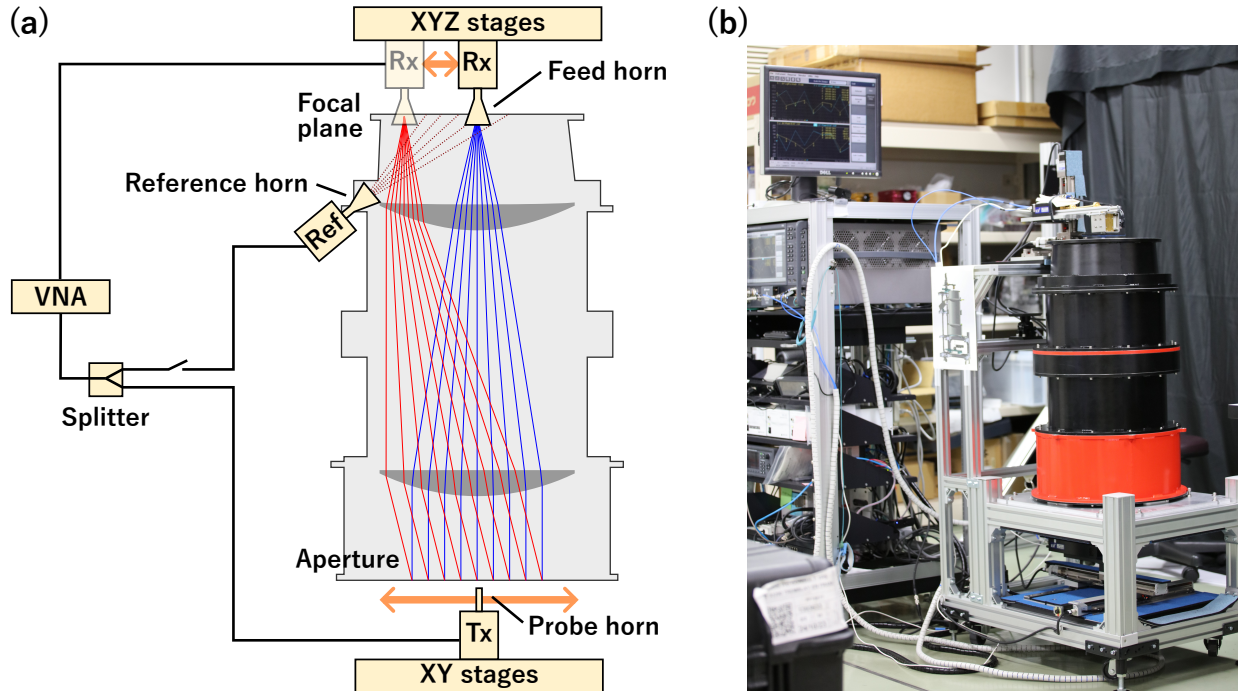


Figure 4. (a) Schematic diagram of the setup for the vector and holographic near-field measurements. The transmitter (Tx) with the probe horn (an open-ended waveguide) is moved by the XY stages and scans the aperture of the ORFPM. The signal is detected at the receiver (Rx) with the feed horn at the focal plane. The feed position can be adjusted by the XYZ stages. For the holographic phase-retrieval measurements, the signal from the reference horn, which is phase-locked with the signal from the probe horn, is turned on. In both measurements, the vector network analyzer (VNA) measures both the intensity and phase of the detected signals, but only the intensity information is analyzed for the phase-retrieval measurements. (b) Photo of the measurement setup.

3.3 Data Reduction

The main principles behind near-field vector as well as holographic phase retrieval measurements have been explained in Section 2. Here, we will provide an explanation of the pipeline that was developed for this work in order to reduce and analyze the data. The code for this pipeline, as well as various analysis tools will be made available on GitHub^{*}.

Every measurement we obtained depended on the scanning spatial resolution as well as the frequency resolution of the measurement. A finer scanning resolution allows to measure higher angles in the farfield pattern, and a better frequency resolution helps with the precision of the holographic phase-retrieval method. This comes at the cost of time, with most near-field measurements taking at least a day to complete. The holographic measurements could take up to one week to complete.

For every measurement, during the scanning of the XY plane we periodically measured the signal at the center to serve as reference measurements. Although taken at the same place in the XY plane, these measurements show some amount of variation that's due to uncontrolled variations of the conditions of the experiment. Changes in atmospheric conditions, such as temperature, were the main factors we wanted to compensate for using these reference measurements. We did so by normalizing the measurements over time using the variations of the reference.

After doing so, we computed the 2D Fourier transform using the **NumPy** *fft* module.¹⁹ Another necessary step in data reduction is to take into account the antenna pattern of the probe horn itself. We used the formulas described in Ref 20 to remove the probe horn's features from the antenna patterns we are trying to characterize. Due to this approximate formula, we limit our antenna patterns up to $\theta = 60^\circ$.

4. RESULTS

4.1 Near-Field

The results of our near-field vector measurements are shown in Fig.5. We used a 0.68 mm spatial resolution to sample the XY plane, as well as measuring 21 frequencies across the 140-220 GHz range. We restricted our plots to the range $\theta \leq 60^\circ$ due to the limitation of the approximation used to correct the probe beam.^{7,20} The dynamic range of this measurement goes up to 80 dB, with some apparent side-lobe patterns at $\theta \approx 30^\circ$ and with a relative intensity compared to the main lobe of -50 dB.

*nearfieldPy

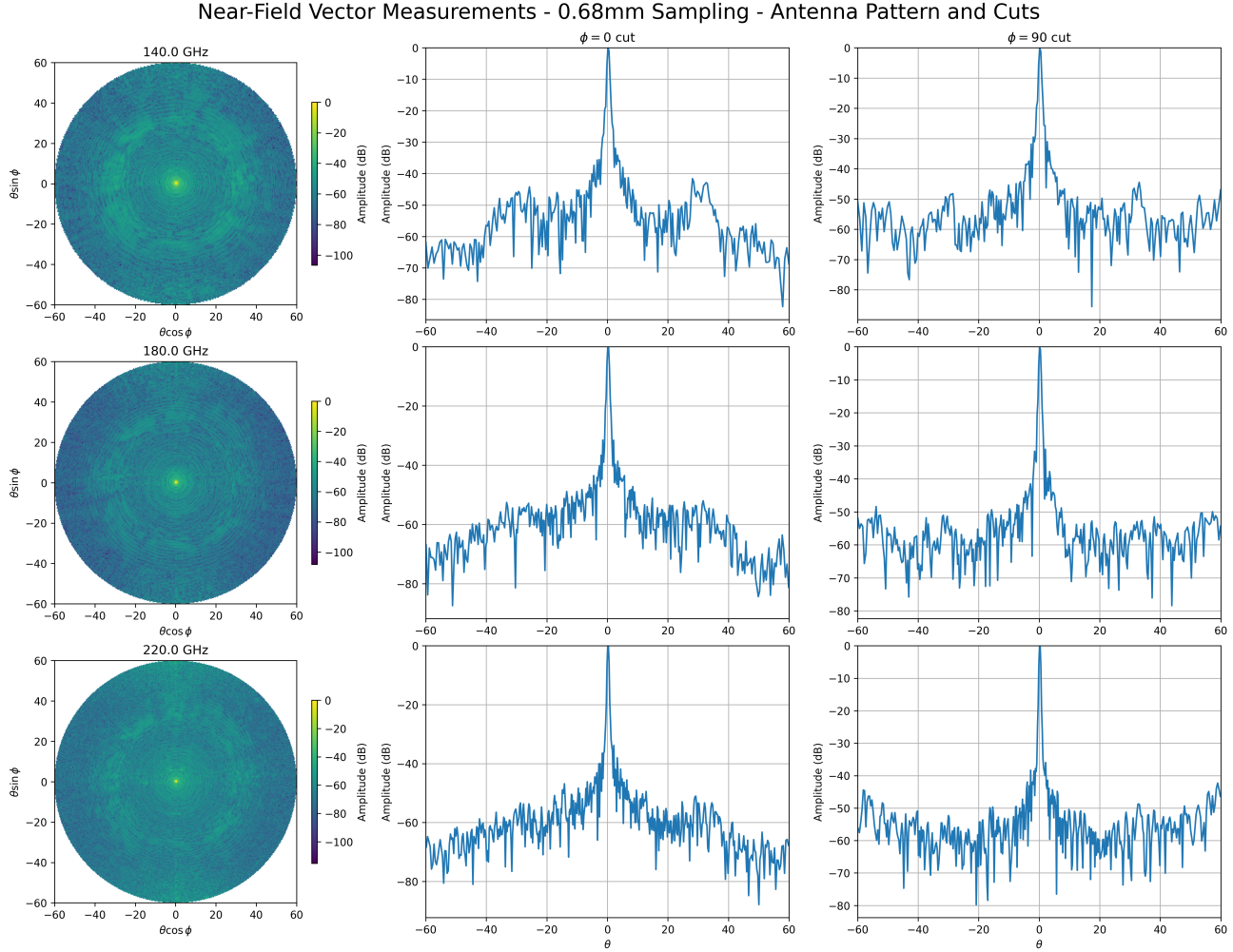


Figure 5. Near-field vector measurements with 0.68mm spatial sampling. Patterns from 140 to 220 GHz have been measured. The plots in each row show the antenna patterns at frequencies 140, 180 and 220 GHz and their cuts across the $\phi = 0$ or $\phi = 90$ axes. The 2D representation is in the $\theta \cos \phi$, $\theta \sin \phi$ polar spherical positioning system.¹² The intensity going back up at high $|\theta|$ in the $\phi = 90$ cuts is an effect of the probe beam correction being less accurate at higher values of $|\theta|$. Other directions are less susceptible to this effect, and the dynamic range of this measurement goes to -80 dB.

4.2 Holographic

The holographic phase retrieval results are presented in figures 6,7,8. When we look at the time-delay spectra presented in figure 6, we see that there are multiple peaks and that their position can be dependent on r . We define a window around $t = 4.5$ ns, with its edges optimized to recover the closest value of the intensity of the recovered signal. That is to say, we iteratively optimize the window function $w(r, t)$ so that the distance $\|E_{sig}^{retrieved}|^2 - |E_{sig}|^2\|$ is minimal. The retrieved amplitudes and phases are presented in figure 7, and the resulting antenna patterns are presented in figure 8.

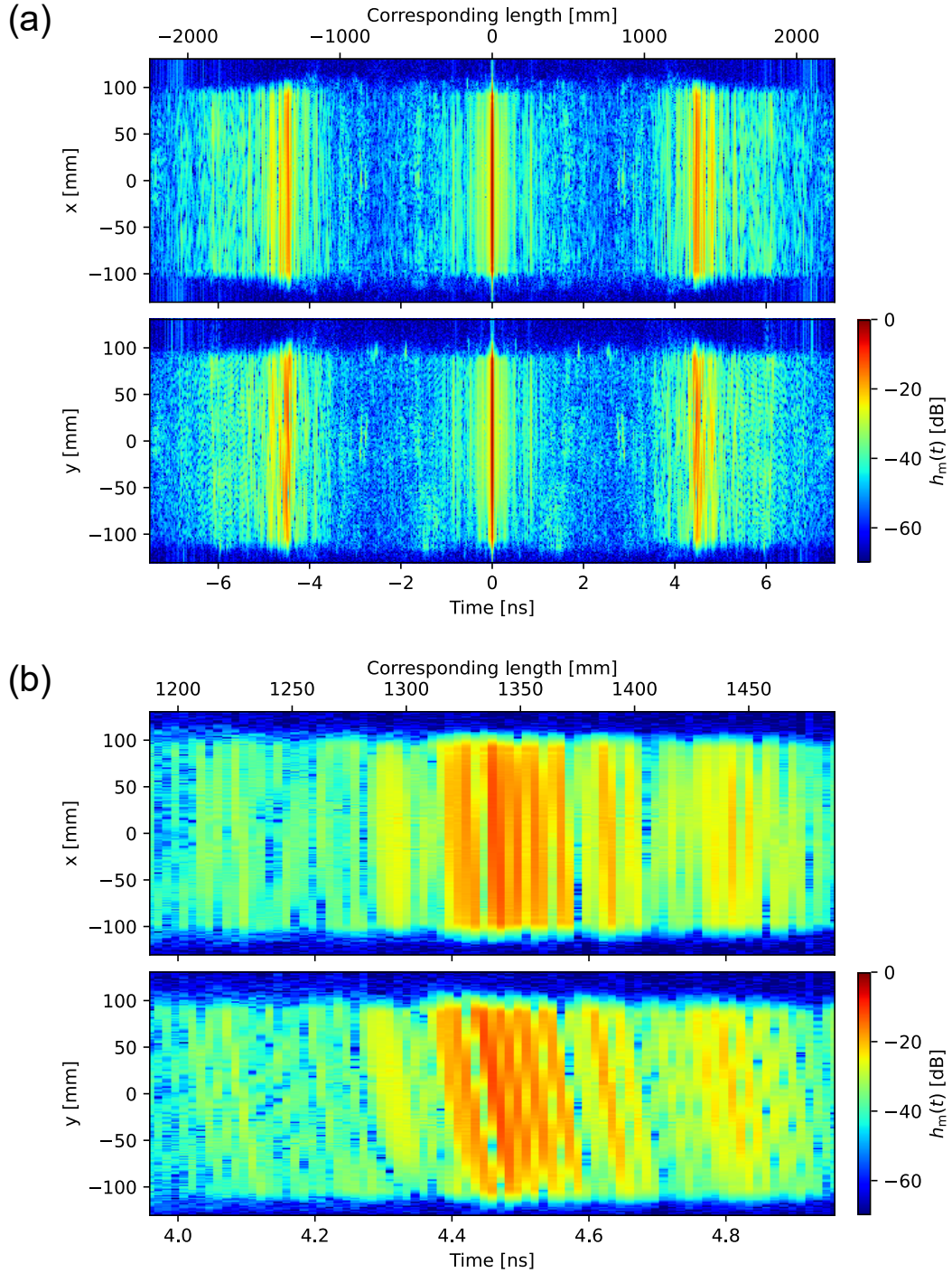


Figure 6. (a) Time profile of the measured hologram. The horizontal axes show the arrival time of each component, computed by inverse Fourier transformation. The vertical axes show the aperture position. (b) Same as (a), but the horizontal axes are from 3.95 ns to 4.95 ns.

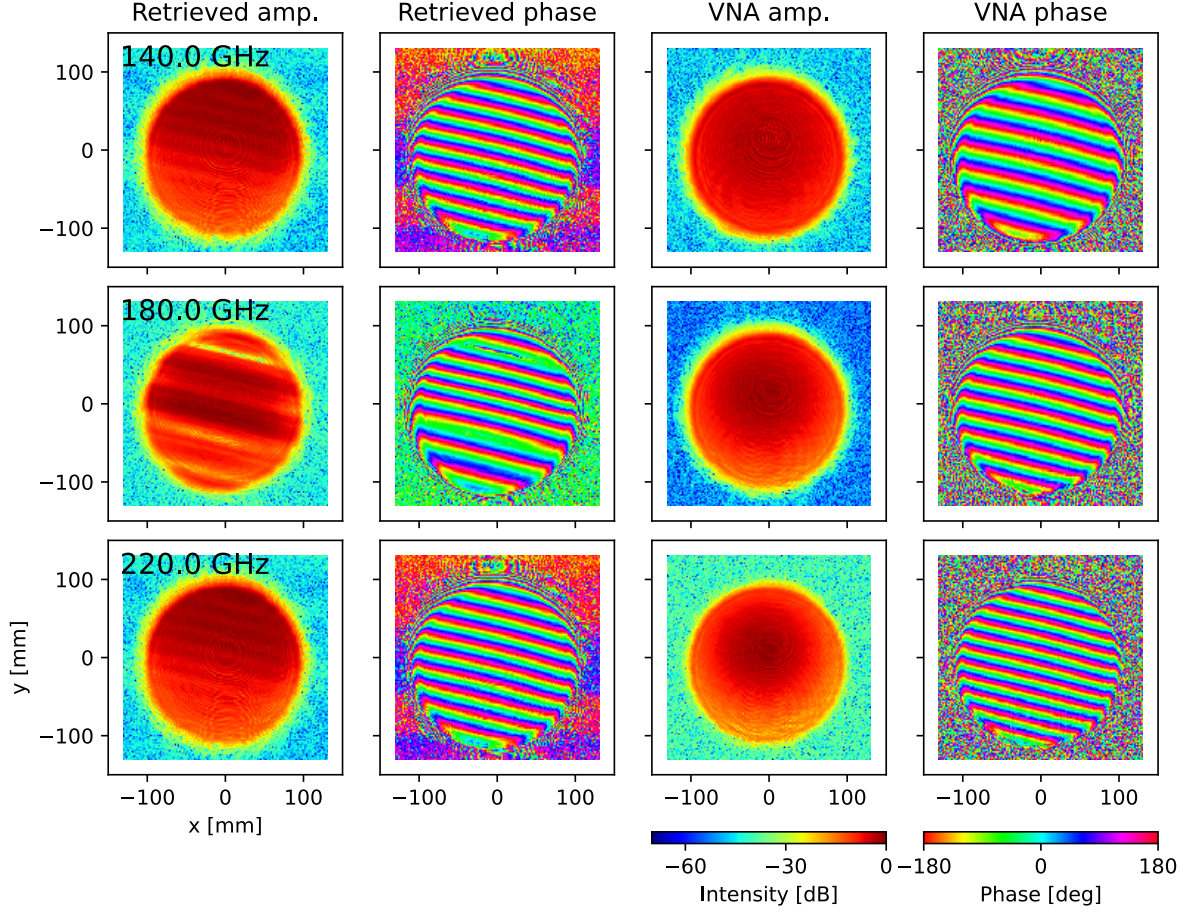


Figure 7. Retrieved and VNA-measured aperture fields at 140, 180 and 220 GHz.

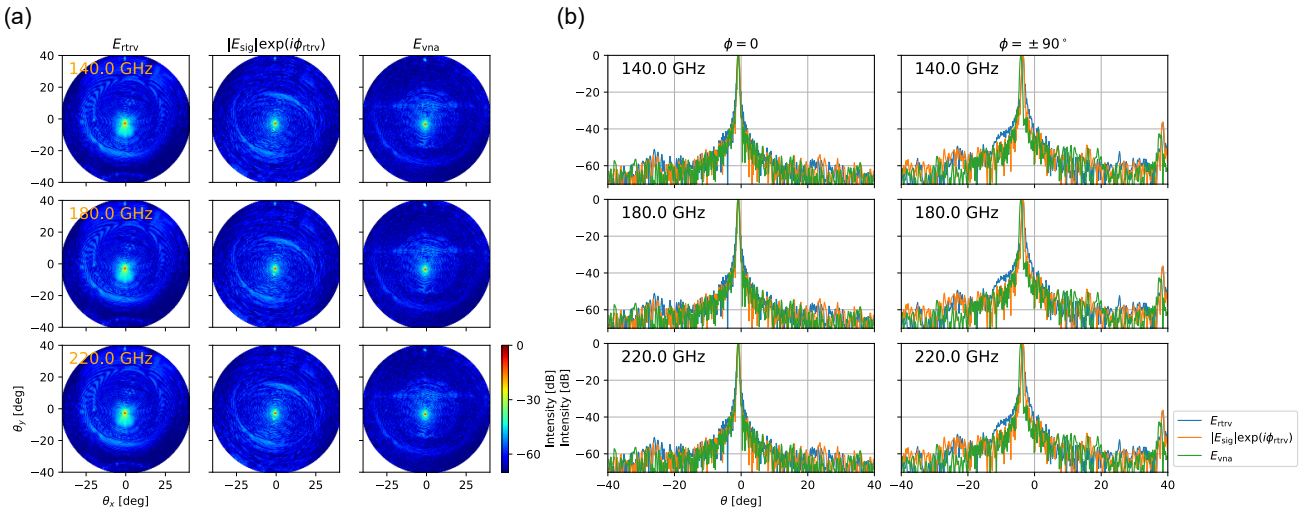


Figure 8. (a) Retrieved (E_{rtrv}) and VNA-measured (E_{vna}) far-field patterns. The patterns in the middle column are computed from the directly-measured aperture intensity ($|E_{\text{sig}}|$) combined with the retrieved aperture phase (ϕ_{rtrv}). (b) Cross-sectional profiles of each far-field pattern in the $\phi = 0$ and 90° directions.

5. DISCUSSION

5.1 Setup Reliability

5.1.1 Residuals

In order to verify the reliability of our measurements and to test the impact of certain systematic effects we can compute the residuals. The residuals, in dB, between two measurements A and B are defined as :

$$\text{residuals}(A, B) = dB\left(\frac{A + B}{2} + |A - B|\right) - dB\left(\frac{A + B}{2}\right) \quad (7)$$

We analyzed the residuals in two cases : one where one measurement is sampled at 1mm and the other at 0.68mm (figure 11), and another where they have the same sampling but do not have the same scanning strategy (figures 9,10). In the first case, due to the sampling difference, the measurements had to be interpolated to the same grid in order to compute the residuals. This interpolation is what causes the important dispersion for beam intensities larger than -30dB. This corresponds to the area close to the main lobe, where there's a lot of variation in intensity in a small angular range. This dispersion is not found in the second case, where both measurements do not need to be interpolated, however the bulk of the distribution of the residuals look the same. Looking at the spatial distribution of the residuals in figure 9 gives some important information on the quality of the measurement. First of all, a cross shape can be seen that we attribute to a scanning strategy systematic effect. We can also see that the residuals are the lowest in the main lobe and the side lobe areas, where we can see the same side lobe morphology appear as in figure 5.

This residuals analysis highlights the precision of our measurement setup :

- The main lobe area (Beam intensity ≥ -20 dB) has residuals under 1 dB, with a small standard deviation
- The side lobe area (Beam intensity ≈ 45 dB) has residuals around 1 dB, with a larger standard deviation than the main lobe
- The residuals steadily increase when the beam intensity gets lower, and at -80 dB they are at around 3 dB, with a 1σ standard deviation of a little under 2 dB.

The residuals can give us an estimation of the signal to noise ratio SNR , although the estimation of the noise is limited by the possible differences between the two measurements used. Using the same binned data as presented in Figure 10, we get a mean value over the antenna pattern of $SNR = 10.7$. In the main lobe area, the SNR is around 30 – 50. In the far sidelobe area, it's around 7 – 8. At the end of the measured dynamic range, around -80 dB, the SNR is very close to 1.

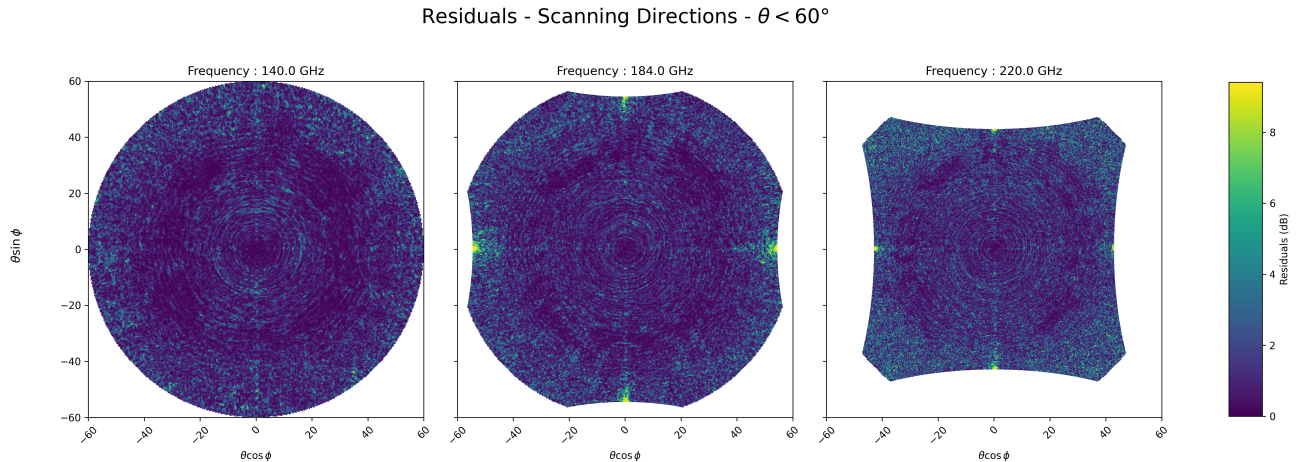


Figure 9. Patterns seen in the plotted residuals between two scanning directions

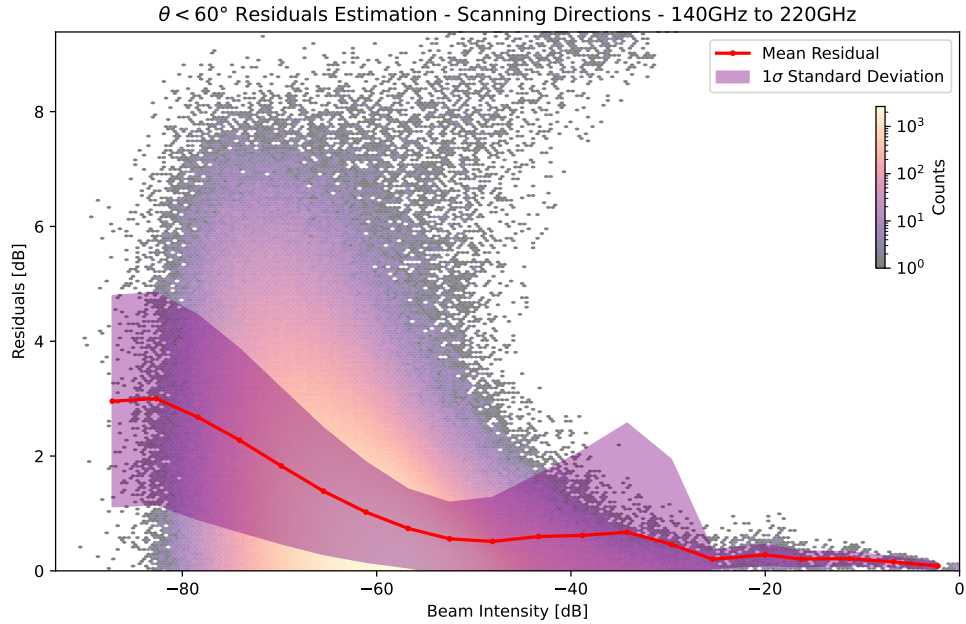


Figure 10. Residuals - Scanning Directions

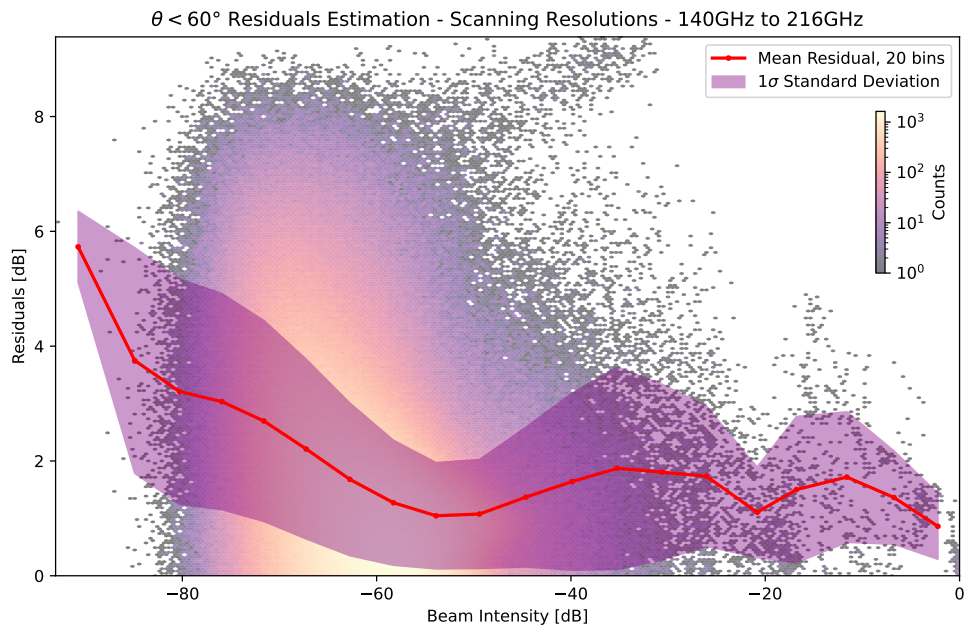


Figure 11. Residuals estimation between a measurement at 1mm sampling and another at 0.68mm sampling.

5.1.2 Side lobe patterns

When analyzing the antenna patterns we obtained, we found that the side lobe patterns looked a lot like the pattern formed by the gaps between the CR110 tiles of the absorber we used inside of the optical system. To

test this out, we replaced these tiles with a smooth layer of AN72 as illustrated in figures 3, 12. The difference in the side lobe patterns between the two setups indicate that they are directly influenced by the geometry of the optical system. In other words, this shows that our measurement setup accurately measures the side lobe features and the properties of the optical system, with only a small impact from the measurement setup. This again reinforces the robustness of the near-field approach to measure side lobe features.

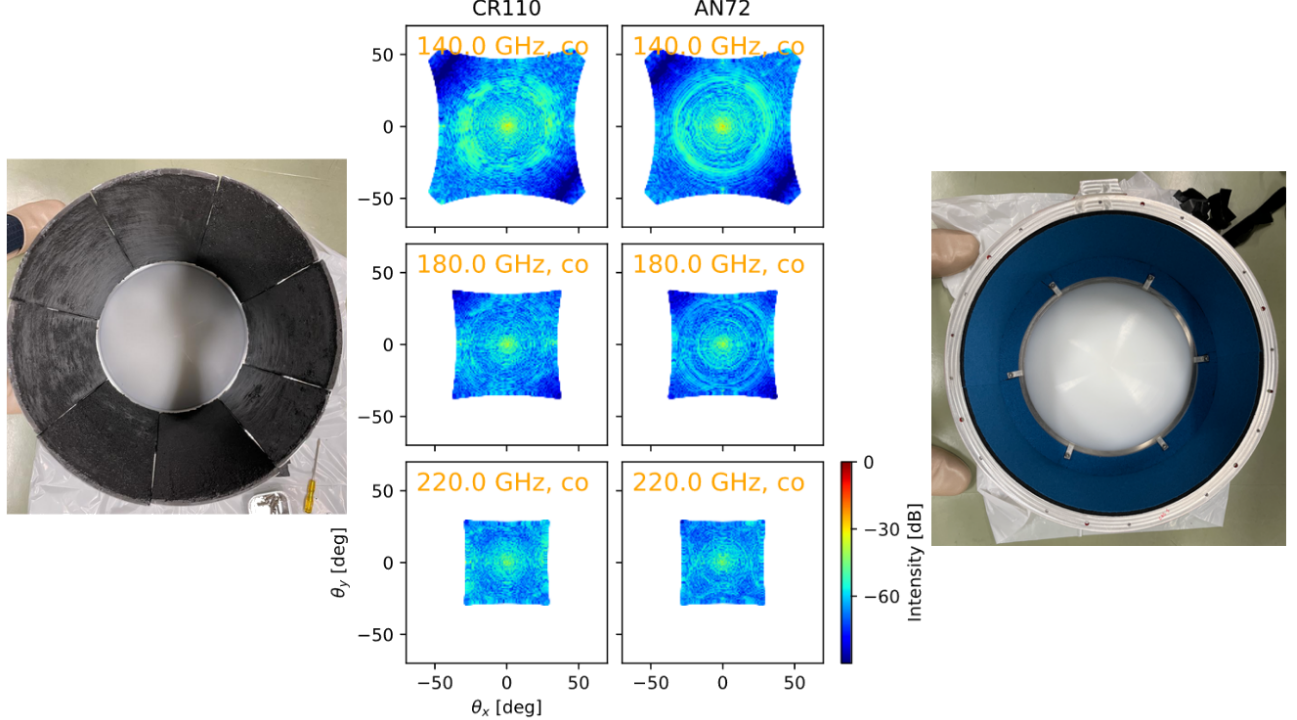


Figure 12. Comparison of the antenna patterns obtained with two different kinds of absorbers. On the left, 8 tiles of CR110 cover the interior of the optical system. On the right, a layer of AN72 covers the interior. The shape of the side lobes is far more regular when using AN72. The shape and the gaps between the tiles can be seen in the side lobe patterns on the left.

5.1.3 Frequency-Time Analysis

By using the CWT to analyse the time-delay spectra of an holographic measurement, we have been able to make a more detailed diagnostic of the measurement setup and the optical prototype. For each frequency band of each measurement, we obtain the CWT time-delay power spectrum, an example of which is shown in figure 13. Though this time-frequency approach can still be developed further, we managed to extract valuable information to better calibrate the setup and understand where our errors could come from. Straylight and multiple reflections in the optical system are identified as possible causes for the broadening of the spectra around $t = 4.5\text{ns}$. On both the reference and the non-holographic measurement we can see that the frequencies around 180-190 GHz are predominant in the power spectrum, which could indicate resonant frequencies for stationary waves in the optical system. Horizontal lines in the reference and hologram power spectrum, around $t = 0.5\text{ns}$ were identified as coming from standing waves in the coaxial cable linked to the VNA. The length of this cable was measured and matched the corresponding time-delay.

This frequency-time analysis also highlights the frequency dependency of the position of the time-delay peak in the wavelet transform of $H'(r, \omega)$. A frequency-dependent window function would be better suited to filter out the components we are not interested in. However, this approach doesn't work with the CWT since the convolution theorem doesn't apply.

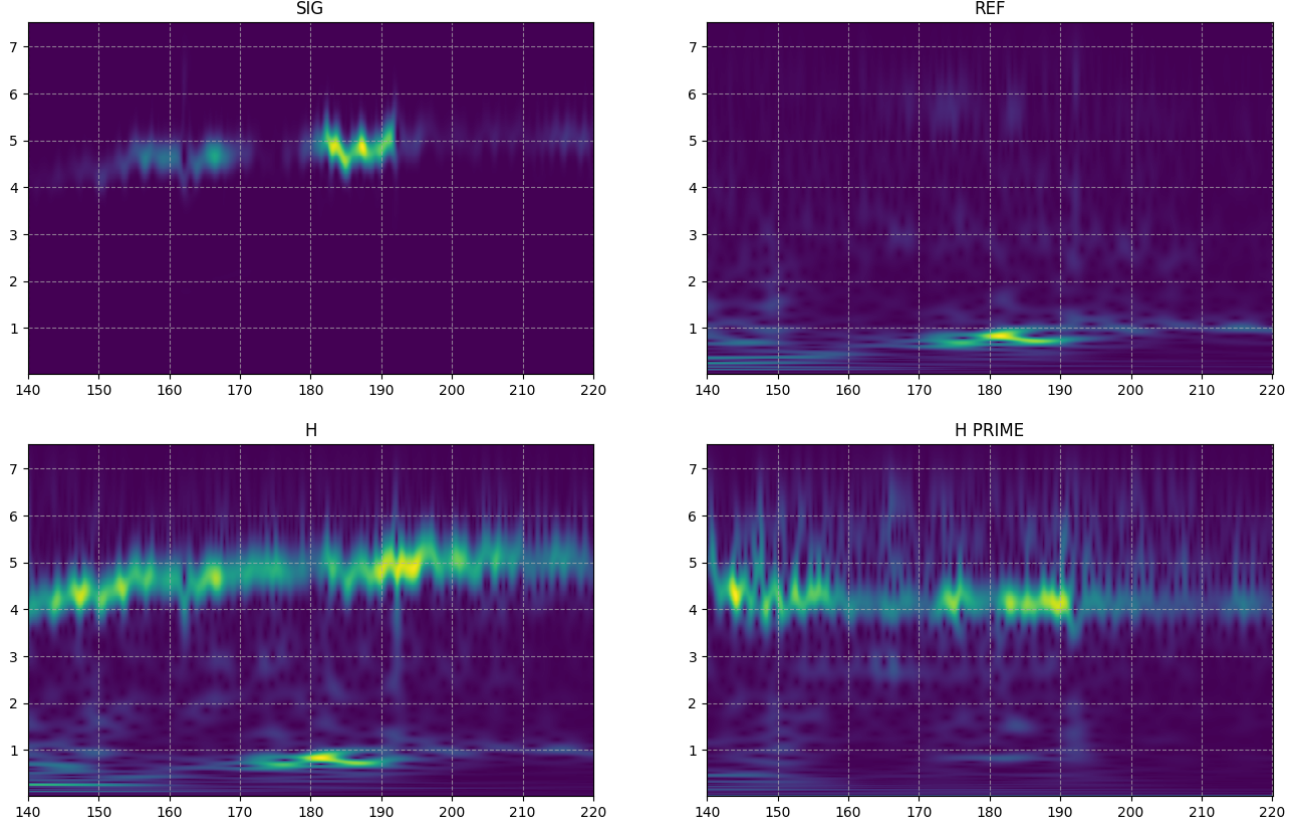


Figure 13. CWT diagnostics of the holographic measurements.

5.2 Comparison with simulations

Physical optics simulations of LiteBIRD’s HFT, with conditions similar to the ones we have with our prototype were performed internally in 2019 by Hiroaki Imada. Figure 14 shows one of the antenna patterns produced for the HFT. The simulations predict side lobes at $\theta = 30^\circ$ with a relative intensity compared to the peak of the main lobe of -50 dB. This corresponds to what we have observed in our near-field vector measurements (5). This reinforces the confidence we have in the quality and the precision of our measurement setup and near-field method.

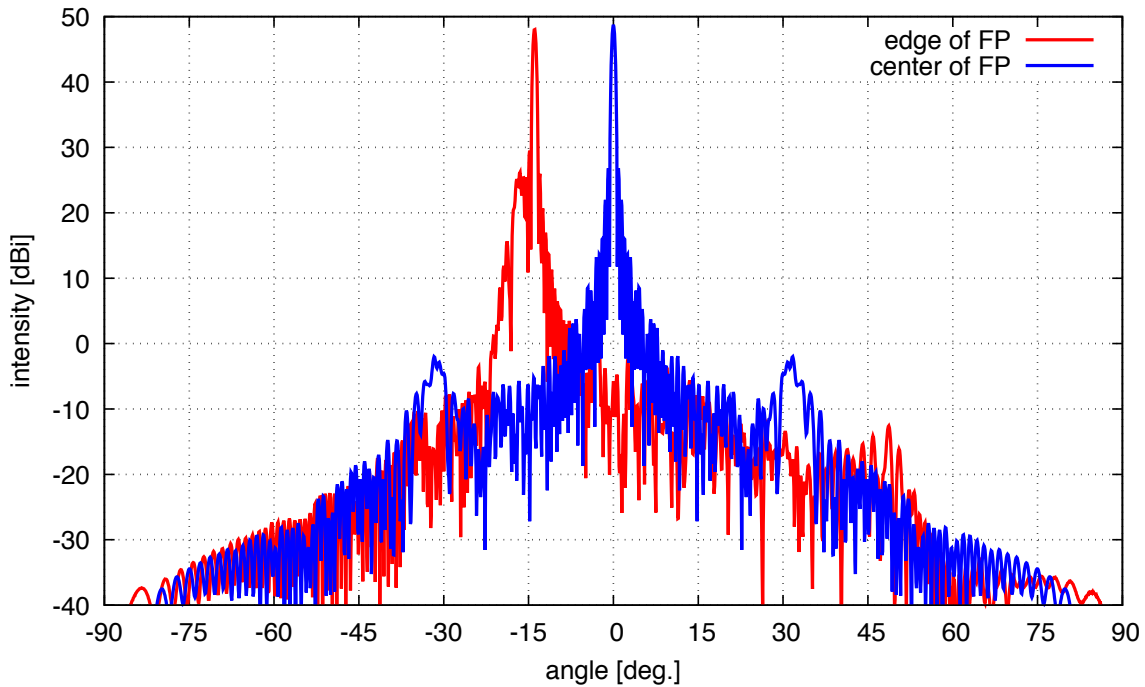


Figure 14. Physical optics simulation of the HFT antenna pattern.

6. CONCLUSION

We have investigated the feasibility of the vector near-field and holographic phase retrieval techniques for the study of LiteBIRD's HFT, following the successful study performed for the LFT. We have managed to verify that such a measurement setup yields robust and accurate data for the characterization of the optical design of the HFT. To do so, we measured the antenna patterns of a prototype of the HFT's optical system using a VNA at frequencies ranging from 140 to 220 GHz. The holographic phase retrieval method looks promising but we have encountered limitations that prevented us from coming to satisfying results with this round of measurements. However, there are ways to improve both the measurement setup as well as the data analysis that we were able to identify thanks to frequency-time analysis of the data. In the case of vector near-field measurements, we have achieved a reliable dynamic range of -80dB as well as antenna patterns going up to $\theta = 60^\circ$. We have detected far side lobe features at $\theta \approx 30^\circ$, with a relative intensity of around -50 dB. These measurements match the physical optics simulations performed on the same optical system. We also have performed an analysis of the measurement's reliability through the estimation of residuals. The residuals on the main beam (less than 1 dB) and the side lobes (95% are below 2 dB) are very small, and all the dynamic range is known with robust precision : points at -80 dB have an average residual of around 3 dB. There are many perspectives in the continuation of this work, both in line with what has been done for the LFT such as straylight analysis as well as new ideas for data analysis that should also be useful for the characterization of the LFT and they will be presented and discussed in a future article.

ACKNOWLEDGMENTS

The authors of this work would like to acknowledge the participation of Andrea Occhiuzzi (Univ Rome Sapienza), Fumiya Miura (Yokohama National Univ and ISAS) and Frederick Matsuda (ISAS) who have joined our discussions on the measurements.

This work was financially supported by MEXT/JSPS KAKENHI Grant Numbers JP17H01115, JP23K25889, JP23K17309 and JP24K17078.

LiteBIRD (phase A) activities are supported by the following funding sources: ISAS/JAXA, MEXT, JSPS, KEK (Japan); CSA (Canada); CNES, CNRS, CEA (France); DFG (Germany); ASI, INFN, INAF (Italy); RCN (Norway); MCIN/AEI, CDTI (Spain); SNSA, SRC (Sweden); UKSA (UK); and NASA, DOE (USA).

REFERENCES

- [1] M. Kamionkowski, A. Kosowsky, and A. Stebbins, “A Probe of Primordial Gravity Waves and Vorticity,” *Physical Review Letters* **78**, pp. 2058–2061, Mar. 1997. Publisher: American Physical Society.
- [2] U. Seljak and M. Zaldarriaga, “Signature of Gravity Waves in the Polarization of the Microwave Background,” *Physical Review Letters* **78**, pp. 2054–2057, Mar. 1997. Publisher: American Physical Society.
- [3] M. Tristram, A. J. Banday, K. M. Górski, R. Keskitalo, C. R. Lawrence, K. J. Andersen, R. B. Barreiro, J. Borrill, L. P. L. Colombo, H. K. Eriksen, R. Fernandez-Cobos, T. S. Kisner, E. Martínez-González, B. Partridge, D. Scott, T. L. Svalheim, and I. K. Wehus, “Improved limits on the tensor-to-scalar ratio using *bicep* and *planck* data,” *Phys. Rev. D* **105**, p. 083524, Apr 2022.
- [4] M. Hazumi, P. A. R. Ade, Y. Akiba, D. Alonso, K. Arnold, J. Aumont, C. Baccigalupi, D. Barron, S. Basak, S. Beckman, J. Borrill, F. Boulanger, M. Bucher, E. Calabrese, Y. Chinone, S. Cho, A. Cukierman, D. W. Curtis, T. de Haan, M. Dobbs, A. Dominjon, T. Dotani, L. Duband, A. Ducout, J. Dunkley, J. M. Duval, T. Ellefot, H. K. Eriksen, J. Errard, J. Fischer, T. Fujino, T. Funaki, U. Fuskeland, K. Ganga, N. Goeckner-Wald, J. Grain, N. W. Halverson, T. Hamada, T. Hasebe, M. Hasegawa, K. Hattori, M. Hattori, L. Hayes, N. Hidehira, C. A. Hill, G. Hilton, J. Hubmayr, K. Ichiki, T. Iida, H. Imada, M. Inoue, Y. Inoue, K. D. Irwin, H. Ishino, O. Jeong, H. Kanai, D. Kaneko, S. Kashima, N. Katayama, T. Kawasaki, S. A. Kernasovskiy, R. Keskitalo, A. Kibayashi, Y. Kida, K. Kimura, T. Kisner, K. Kohri, E. Komatsu, K. Komatsu, C. L. Kuo, N. A. Kurinsky, A. Kusaka, A. Lazarian, A. T. Lee, D. Li, E. Linder, B. Maffei, A. Mangilli, M. Maki, T. Matsumura, S. Matsuura, D. Meilhan, S. Mima, Y. Minami, K. Mitsuda, L. Montier, M. Nagai, T. Nagasaki, R. Nagata, M. Nakajima, S. Nakamura, T. Namikawa, M. Naruse, H. Nishino, T. Nitta, T. Noguchi, H. Ogawa, S. Oguri, N. Okada, A. Okamoto, T. Okamura, C. Otani, G. Patanchon, G. Pisano, G. Rebeiz, M. Remazeilles, P. L. Richards, S. Sakai, Y. Sakurai, Y. Sato, N. Sato, M. Sawada, Y. Segawa, Y. Sekimoto, U. Seljak, B. D. Sherwin, T. Shimizu, K. Shinozaki, R. Stompor, H. Sugai, H. Sugita, A. Suzuki, J. Suzuki, O. Tajima, S. Takada, R. Takaku, S. Takakura, S. Takatori, D. Tanabe, E. Taylor, K. L. Thompson, B. Thorne, T. Tomaru, T. Tomida, N. Tomita, M. Tristram, C. Tucker, P. Turin, M. Tsujimoto, S. Uozumi, S. Utsunomiya, Y. Uzawa, F. Vansyngel, I. K. Wehus, B. Westbrook, M. Willer, N. Whitehorn, Y. Yamada, R. Yamamoto, N. Yamasaki, T. Yamashita, and M. Yoshida, “LiteBIRD: A satellite for the studies of b-mode polarization and inflation from cosmic background radiation detection,” *194*(5), pp. 443–452.
- [5] Y. Sekimoto, P. A. R. Ade, A. Adler, E. Ally, K. Arnold, D. Auguste, J. Aumont, R. Aurlien, J. Austermann, C. Baccigalupi, A. J. Banday, R. Banerji, R. B. Barreiro, S. Basak, J. Beall, D. Beck, S. Beckman, J. Bermejo, P. de Bernardis, M. Bersanelli, J. Bonis, J. Borrill, F. Boulanger, S. Bounissou, M. Brilenkov, M. Brown, M. Bucher, E. Calabrese, P. Campeti, A. Carones, F. J. Casas, A. Challinor, V. Chan, K. Cheung, Y. Chinone, J. F. Cliche, L. Colombo, F. Columbro, J. Cubas, A. Cukierman, D. Curtis, G. D’Alessandro, N. Dachlythra, M. D. Petris, C. Dickinson, P. Diego-Palazuelos, M. Dobbs, T. Dotani, L. Duband, S. Duff, J. M. Duval, K. Ebisawa, T. Ellefot, H. K. Eriksen, J. Errard, T. Essinger-Hileman, F. Finelli, R. Flauger, C. Franceschet, U. Fuskeland, M. Galloway, K. Ganga, J. R. Gao, R. Genova-Santos, M. Gerbino, M. Gervasi, T. Ghigna, E. Gjerløw, M. L. Gradziel, J. Grain, F. Grupp, A. Gruppuso, J. E. Gudmundsson, T. de Haan, N. W. Halverson, P. Hargrave, T. Hasebe, M. Hasegawa, M. Hattori, M. Hazumi, S. Henrot-Versillé, D. Herman, D. Herranz, C. A. Hill, G. Hilton, Y. Hirota, E. Hivon, R. A. Hlozek, Y. Hoshino, E. de la Hoz, J. Hubmayr, K. Ichiki, T. iida, H. Imada, K. Ishimura, H. Ishino, G. Jaehnig, T. Kaga, S. Kashima, N. Katayama, A. Kato, T. Kawasaki, R. Keskitalo, T. Kisner, Y. Kobayashi, N. Kogiso, A. Kogut, K. Kohri, E. Komatsu, K. Komatsu, K. Konishi, N. Krachmalnicoff, I. Kreykenbohm, C. L. Kuo, A. Kushino, L. Lamagna, J. V. Lanen, M. Lattanzi, A. T. Lee, C. Leloup, F. Levrier, E. Linder, T. Louis, G. Luzzi, T. Maciaszek, B. Maffei, D. Maino, M. Maki, S. Mandelli, E. Martinez-Gonzalez, S. Masi, T. Matsumura, A. Mennella, M. Migliaccio, Y. Minanmi, K. Mitsuda, J. Montgomery, L. Montier, G. Morgante, B. Mot, Y. Murata, J. A. Murphy, M. Nagai, Y. Nagano, T. Nagasaki, R. Nagata, S. Nakamura, T. Namikawa, P. Natoli, S. Nerval, T. Nishibori, H. Nishino, C. O’Sullivan, H. Ogawa, H. Ogawa, S. Oguri, H. Ohsaki, I. S. Ohta, N. Okada, N. Okada, L. Pagano, A. Paiella, D. Paoletti, G. Patanchon,

- J. Peloton, F. Piacentini, G. Pisano, G. Polenta, D. Poletti, T. Prouvé, G. Puglisi, D. Rambaud, C. Raum, S. Realini, M. Reinecke, M. Remazeilles, A. Ritacco, G. Roudil, J. A. Rubino-Martin, M. Russell, H. Sakurai, Y. Sakurai, M. Sandri, M. Sasaki, G. Savini, D. Scott, J. Seibert, B. Sherwin, K. Shinozaki, M. Shiraishi, P. Shirron, G. Signorelli, G. Smecher, S. Stever, R. Stompor, H. Sugai, S. Sugiyama, A. Suzuki, J. Suzuki, T. L. Svalheim, E. Switzer, R. Takaku, H. Takakura, S. Takakura, Y. Takase, Y. Takeda, A. Tartari, E. Taylor, Y. Terao, H. Thommesen, K. L. Thompson, B. Thorne, T. Toda, M. Tomasi, M. Tominaga, N. Trappe, M. Tristram, M. Tsuji, M. Tsujimoto, C. Tucker, J. Ullom, G. Vermeulen, P. Vielva, F. Villa, M. Vissers, N. Vittorio, I. Wehus, J. Weller, B. Westbrook, J. Wilms, B. Winter, E. J. Wollack, N. Y. Yamasaki, T. Yoshida, J. Yumoto, M. Zannoni, and A. Zonca, “Concept design of low frequency telescope for CMB B-mode polarization satellite LiteBIRD,” in *Millimeter, Submillimeter, and Far-Infrared Detectors and Instrumentation for Astronomy X*, J. Zmuidzinas and J.-R. Gao, eds., **11453**, p. 1145310, International Society for Optics and Photonics, SPIE, 2020.
- [6] C. Leloup, G. Patanchon, J. Errard, C. Franceschet, J. E. Gudmundsson, S. Henrot-Versillé, H. Imada, H. Ishino, T. Matsumura, G. Puglisi, W. Wang, A. Adler, J. Aumont, R. Aurlien, C. Baccigalupi, M. Ballardini, A. J. Banday, R. B. Barreiro, N. Bartolo, A. Basyrov, M. Bersanelli, D. Blinov, M. Bortolami, T. Brinckmann, P. Campeti, A. Carones, F. Carralot, F. J. Casas, K. Cheung, L. Clermont, F. Columbro, G. Conenna, A. Coppolecchia, F. Cuttaia, G. D’Alessandro, P. de Bernardis, T. de Haan, M. D. Petris, S. D. Torre, P. Diego-Palazuelos, H. K. Eriksen, F. Finelli, U. Fuskeland, G. Galloni, M. Galloway, M. Georges, M. Gerbino, M. Gervasi, R. T. Génova-Santos, T. Ghigna, S. Giardiello, C. Gimeno-Amo, E. Gjerløw, A. Gruppuso, M. Hazumi, L. T. Hergt, D. Herranz, E. Hivon, T. D. Hoang, B. Jost, K. Kohri, N. Krachmalnicoff, A. T. Lee, M. Lembo, F. Levrier, A. I. Lonappan, M. López-Caniego, J. Macias-Perez, E. Martínez-González, S. Masi, S. Matarrese, S. Micheli, M. Monelli, L. Montier, G. Morgante, B. Mot, L. Mousset, T. Namikawa, P. Natoli, A. Novelli, F. Noviello, I. Obata, K. Odagiri, L. Pagano, A. Paiella, D. Paoletti, G. Pascual-Cisneros, V. Pavlidou, F. Piacentini, G. Piccirilli, G. Pisano, G. Polenta, N. Raffuzzi, M. Remazeilles, A. Ritacco, A. Rizzieri, M. Ruiz-Granda, Y. Sakurai, M. Shiraishi, S. L. Stever, Y. Takase, K. Tassis, L. Terenzi, K. L. Thompson, M. Tristram, L. Vacher, P. Vielva, I. K. Wehus, G. Weymann-Despres, M. Zannoni, and Y. Zhou, “Impact of beam far side-lobe knowledge in the presence of foregrounds for litebird,” 2023.
- [7] H. Takakura, Y. Sekimoto, J. Inatani, S. Kashima, H. Imada, T. Hasebe, T. Kaga, Y. Takeda, and N. Okada, “Far-sidelobe antenna pattern measurement of LiteBIRD low frequency telescope in 1/4 scale,” **9**(6), pp. 598–605. Conference Name: IEEE Transactions on Terahertz Science and Technology.
- [8] H. Takakura, Y. Sekimoto, J. Inatani, S. Kashima, M. Sugimoto, R. Nakano, and R. Nagata, “Wide-field polarization angle measurements of a LiteBIRD low-frequency telescope scaled antenna,” **9**(2), p. 024003. Publisher: SPIE.
- [9] R. Nakano, H. Takakura, Y. Sekimoto, J. Inatani, M. Sugimoto, S. Oguri, and F. Matsuda, “Holographic phase-retrieval method of near-field antenna pattern measurement for bolometer-array-equipped millimeter-wave telescopes,” **9**(2), p. 028003. Publisher: SPIE.
- [10] L. Lamagna, C. Franceschet, M. D. Petris, J. E. Gudmundsson, P. Hargrave, B. Maffei, F. Noviello, C. O’Sullivan, A. Paiella, F. Columbro, J. Austermann, M. Bersanelli, A. Chahadieh, M. Cicuttin, L. Clermont, P. de Bernardis, K. Fleury-Frenette, M. P. Georges, C. Geuzaine, J. Hastanin, S. Henrot-Versillé, J. Hubmayr, G. Jaehnig, R. Keskitalo, S. Masi, F. Matsuda, T. Matsumura, L. Montier, B. Mot, F. Piacentini, G. Pisano, J. Y. Plesseria, A. Ritacco, G. Savini, A. Shitsov, A. Suzuki, N. Trappe, and B. Winter, “Optical modeling for the LiteBIRD Medium and High Frequency Telescope,” in *Millimeter, Submillimeter, and Far-Infrared Detectors and Instrumentation for Astronomy XI*, J. Zmuidzinas and J.-R. Gao, eds., **12190**, p. 121901R, International Society for Optics and Photonics, SPIE, 2022.
- [11] D. Paris, W. Leach, and E. Joy, “Basic theory of probe-compensated near-field measurements,” *IEEE Transactions on Antennas and Propagation* **26**(3), pp. 373–379, 1978.
- [12] C. Parini, S. Gregson, J. McCormick, D. J. van Rensburg, and T. Eibert, *Theory and Practice of Modern Antenna Range Measurements, 2nd Expanded Edition, Volume 1*, Electromagnetic Waves, Institution of Engineering and Technology, 2020.
- [13] L. Collaboration, E. Ally, K. Arnold, J. Aumont, R. Aurlien, S. Azzoni, C. Baccigalupi, A. J. Banday, R. Banerji, R. B. Barreiro, N. Bartolo, L. Bautista, D. Beck, S. Beckman, M. Bersanelli, F. Boulanger,

- M. Brilenkov, M. Bucher, E. Calabrese, P. Campeti, A. Carones, F. J. Casas, A. Catalano, V. Chan, K. Cheung, Y. Chinone, S. E. Clark, F. Columbro, G. D'Alessandro, P. de Bernardis, T. de Haan, E. de la Hoz, M. De Petris, S. Della Torre, P. Diego-Palazuelos, M. Dobbs, T. Dotani, J. M. Duval, T. Ellefot, H. K. Eriksen, J. Errard, T. Essinger-Hileman, F. Finelli, R. Flauger, C. Franceschet, U. Fuskeland, M. Galloway, K. Ganga, M. Gerbino, M. Gervasi, R. T. Génova-Santos, T. Ghigna, S. Giardiello, E. Gjerløw, J. Grain, F. Grupp, A. Gruppuso, J. E. Gudmundsson, N. W. Halverson, P. Hargrave, T. Hasebe, M. Hasegawa, M. Hazumi, S. Henrot-Versillé, B. Hensley, L. T. Hergt, D. Herman, E. Hivon, R. A. Hlozek, A. L. Hornsby, Y. Hoshino, J. Hubmayr, K. Ichiki, T. Iida, H. Imada, H. Ishino, G. Jaehnig, N. Katayama, A. Kato, R. Keskitalo, T. Kisner, Y. Kobayashi, A. Kogut, K. Kohri, E. Komatsu, K. Komatsu, K. Konishi, N. Krachmalnicoff, C. L. Kuo, L. Lamagna, M. Lattanzi, A. T. Lee, C. Leloup, F. Levrier, E. Linder, G. Luzzi, J. Macias-Perez, T. Maciaszek, B. Maffei, D. Maino, S. Mandelli, E. Martínez-González, S. Masi, M. Massa, S. Matarrese, F. T. Matsuda, T. Matsumura, L. Mele, M. Migliaccio, Y. Minami, A. Moggi, J. Montgomery, L. Montier, G. Morgante, B. Mot, Y. Nagano, T. Nagasaki, R. Nagata, R. Nakano, T. Namikawa, F. Nati, P. Natoli, S. Nerval, F. Noviello, K. Odagiri, S. Oguri, H. Ohsaki, L. Pagano, A. Paiella, D. Paoletti, A. Passerini, G. Patanchon, F. Piacentini, M. Piat, G. Pisano, G. Polenta, D. Poletti, T. Prouvé, G. Puglisi, D. Rambaud, C. Raum, S. Realini, M. Reinecke, M. Remazeilles, A. Ritacco, G. Roudil, J. A. Rubino-Martin, M. Russell, H. Sakurai, Y. Sakurai, M. Sasaki, D. Scott, Y. Sekimoto, K. Shinozaki, M. Shiraishi, P. Shirron, G. Signorelli, F. Spinella, S. Stever, R. Stompor, S. Sugiyama, R. M. Sullivan, A. Suzuki, T. L. Svalheim, E. Switzer, R. Takaku, H. Takakura, Y. Takase, A. Tartari, Y. Terao, J. Thermeau, H. Thommesen, K. L. Thompson, M. Tomasi, M. Tominaga, M. Tristram, M. Tsuji, M. Tsujimoto, L. Vacher, P. Vielva, N. Vittorio, W. Wang, K. Watanuki, I. K. Wehus, J. Weller, B. Westbrook, J. Wilms, B. Winter, E. J. Wollack, J. Yumoto, and M. Zannoni, “Probing cosmic inflation with the LiteBIRD cosmic microwave background polarization survey,” **2023**(4), p. 042F01.
- [14] G. Junkin, T. Huang, and J. Bennett, “Holographic testing of terahertz antennas,” *IEEE Transactions on Antennas and Propagation* **48**(3), pp. 409–417, 2000.
 - [15] H. Takakura, R. Nakano, Y. Sekimoto, J. Inatani, M. Sugimoto, F. Matsuda, and S. Oguri, “Straylight identification of a crossed-dragone telescope by time-gated near-field antenna pattern measurements,” p. 231, 08 2022.
 - [16] S. Mallat, *A wavelet tour of signal processing : the sparse way*, third edition.. ed., 2009.
 - [17] I. Daubechies, “The wavelet transform, time-frequency localization and signal analysis,” **36**(5), pp. 961–1005. Conference Name: IEEE Transactions on Information Theory.
 - [18] Z. R. Claytor, J. L. van Saders, J. Llama, P. Sadowski, B. Quach, and E. Avallone, “Recovery of TESS stellar rotation periods using deep learning,” **927**(2), p. 219.
 - [19] C. R. Harris, K. J. Millman, S. J. van der Walt, R. Gommers, P. Virtanen, D. Cournapeau, E. Wieser, J. Taylor, S. Berg, N. J. Smith, R. Kern, M. Picus, S. Hoyer, M. H. van Kerkwijk, M. Brett, A. Haldane, J. F. del Río, M. Wiebe, P. Peterson, P. Gérard-Marchant, K. Sheppard, T. Reddy, W. Weckesser, H. Abbasi, C. Gohlke, and T. E. Oliphant, “Array programming with NumPy,” *Nature* **585**, pp. 357–362, Sept. 2020.
 - [20] A. Yaghjian, “Approximate formulas for the far field and gain of open-ended rectangular waveguide,” *IEEE Transactions on Antennas and Propagation* **32**(4), pp. 378–384, 1984.